Microscopic origin of pressure-induced isosymmetric transitions in fluoromanganate cryolites

Nenian Charles[1,*] and James M. Rondinelli[1,2,†]

[1]*Department of Materials Science and Engineering, Drexel University, Philadelphia, Pennsylvania 19104, USA*

[2]*Department of Materials Science and Engineering, Northwestern University, Evanston, Illinois 60208, USA*

(Received 14 May 2014; revised manuscript received 8 August 2014; published 24 September 2014)

Using first-principles density functional theory calculations, we investigate the hydrostatic pressure-induced reorientation of the Mn-F Jahn-Teller bond axis in the fluoride cryolite Na_3MnF_6. We find that a first-order isosymmetric phase transition (IPT) occurs between crystallographically equivalent monoclinic structures at approximately 2.15 GPa, consistent with earlier experimental studies. Mode-crystallography analyses of the pressure-dependent structures in the vicinity of the transition reveal a clear evolution of the Jahn-Teller bond distortions in cooperation with an asymmetrical stretching of the equatorial fluorine atoms in the MnF_6 octahedral units. We identify a significant (70%) change in the orbital occupancy of the e_g manifold of the $3d^4$ Mn(III) to be responsible for the transition, stabilizing one monoclinic $P2_1/n$ variant over the other. The orbital reconstruction as a driving force for the transition is confirmed by analogous calculations of isostructural $3d^0$ Na_3ScF_6, which shows no evidence of an IPT up to 6.82 GPa.

DOI: 10.1103/PhysRevB.90.094114 PACS number(s): 61.50.Ks, 74.62.Fj, 71.15.Mb

I. INTRODUCTION

Perovskite transition-metal compounds with ABX_3 stoichiometry, where X is either oxygen or fluorine, have been extensively studied owing to their ability to support a rich set of physical phenomena ranging from multiferroisim to superconductivity [1–4]. Many of these properties are a direct consequence of structural phase transitions and symmetry reductions, which alter chemical bonding pathways and electronic properties through distortions and rotations of BX_6 octahedra through strong electron-lattice coupling. Indeed, the physical properties of perovskites can be tailored by changing the bonding environments by manipulating the BX_6 size, shape, and connectivity [5] using chemical pressure or epitaxial strain [6–9]. Thus, for electronic function engineering purposes it is useful to understand the tendency of a perovskite to distort, or undergo a structural transitions, which can be estimated using the Goldschmidt tolerance factor [10].

The tremendous success of perovskites has sparked interest in a closely related set of materials, the $A_2BB'X_6$ double perovskites with multiple cations that order among various planes in a periodic fashion (Fig. 1). The additional degree of freedom from compositional ordering not found in simple perovskites [11,12] can be used to obtain desirable ferroic responses [13,14] and explore correlated electron properties [15–17]. It is important to note that while there are a multitude of studies on perovskites and double perovskites, most of the materials physics literature is keenly focused on $X = O$ transition-metal oxides [1]. Fluoride compounds, however, also show an affinity for functional electronic behavior, including mutiferroicity [18–21] and ionic conductivity [22]. Yet these ternary fluorides have received considerably less attention than their oxide counterparts although they are ferroelastic [23] and exhibit polymorphism [24]. As such, their properties are structure and symmetry dependent, albeit they tend to adopt the ideal undistorted structure more frequently [25].

For the case of rock salt ordered double perovskites with two possible B cations (B and B') with $X = F$ (fluorine), these compounds are generally referred to by one of the two prototypes illustrated in Fig. 1. The first class is *cryolite*, after the compound Na_3AlF_6 [26]. This family contains compounds with 12-coordinate A sites, whereby the same cation on the A site is chemically identical to one at the octahedrally coordinated B site ($A = B$), while the B' cation remains unique. This results in the stoichiometry $A_3B'F_6$ for cryolite, and as a result the B cation interactions are "interrupted" by the A cation occupying the B sublattice. The other prototype is *elpasolite*, which is named for the mineral K_2NaAlF_6 [27]. It also refers to structures with 12-fold coordinated A cations, but unlike cryolite, the two octahedrally coordinated B sites are chemically distinct species (B and B') [28,29]. Thus, the stoichiometry for elpasolite is $A_2BB'F_6$.

Here we focus on the cryolite Na_3MnF_6 (tolerance factor of 0.89), which possesses a strong first-order active Jahn-Teller d^4 Mn^{3+} cation and exhibits a distorted monoclinic $P2_1/n$ (space group 14) structure with both in-phase and out-of-phase MnF_6 octahedral rotations in its ground state (Fig. 2) [30]. It is ferroelastic and experimentally undergoes an isostructural first-order monoclinic-to-monoclinic phase transition with hydrostatic pressure [31]. Such isostructural/isosymmetric phase transitions (IPTs) without symmetry reductions [32] infrequently occur in inorganic condensed-matter phases; displacive transitions are much more common [33]. Microscopic origins for such transitions include spin-state transitions [34], electronic or magnetic polarization rotation [35], or bond reconfigurations due to mechanical epitaxial strain constraints [36–40]. For example, IPTs in Mn-based complex oxides have been reported to be induced by chemical pressure [41], surface effects in nanoparticles [42], and thermal cycling by melting an orbitally ordered state [43]. In such cases, the driving force is either a reduction in an electric polarization ($YMnO_3$) or due to the *removal* of the Jahn-Teller distortion altogether.

*neniancharles@drexel.edu

†jrondinelli@northwestern.edu

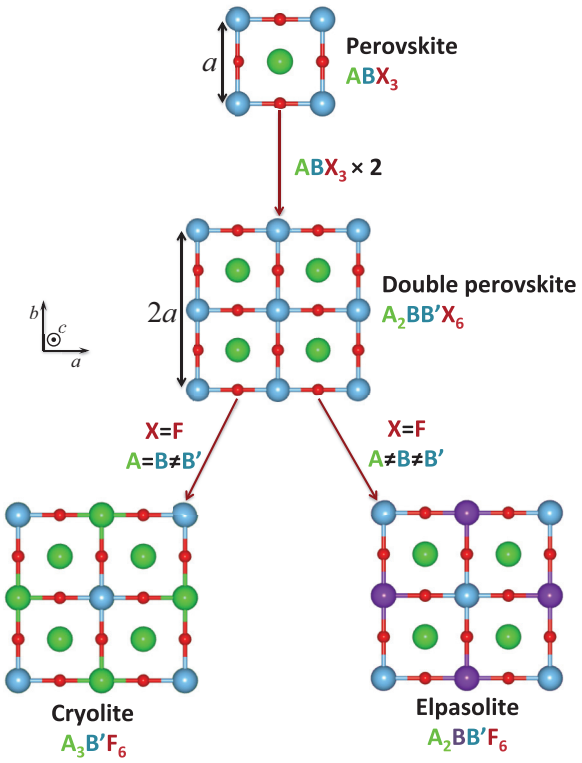

FIG. 1. (Color online) Ideal structures of the double perovskite fluorides cryolite ($A_3B'F_6$, left) and elpasolite ($A_2BB'F_6$, right) as they relate to the cubic ABX_3 perovskite structure (top).

The IPT in Na_3MnF_6 is experimentally found to be reversible while showing characteristic first-order hysteric behavior. Above and below the critical pressure value for the phase transition, the authors of Ref. [31] identified that the short and long Mn-F bond lengths, which are signatures of the Jahn-Teller distortion, persisted across the transition. Unlike the related oxides, the bond distortions remain and only the relative orientation of the distorted bond pairs with respect to the monoclinic axes switch. What are the atomic and electronic features responsible for the phase transition?

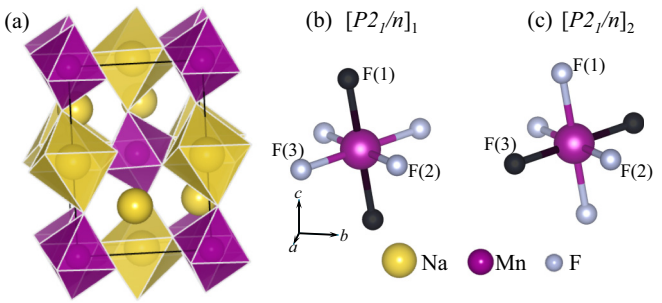

FIG. 2. (Color online) Equilibrium 0 K structure of Na_3MnF_6 (a) and the MnF_6 octahedra of the (b) low-pressure $[P2_1/n]_1$ and (c) high-pressure $[P2_1/n]_2$, phases. The long Mn-F bond axis, referred in the text as the Jahn-Teller (JT) bond axis, is highlighted in black and the ferrodistortive packing of these octahedra along the c axis is the distinguishing structural feature across the monoclinic-to-monoclinic transition.

Is it due to spontaneous strain, the Mn electronic degrees of freedom, or strong electron-lattice interactions? We are unaware of a theory that captures the microscopic origin of this IPT in Na_3MnF_6 or related manganites where the Jahn-Teller distortion is not removed across the isosymmetric transition.

Herein we use density functional theory calculations to identify the microscopic origin of the pressure-induced IPT in the fluoromanganate Na_3MnF_6. We find that the ground-state monoclinic structure is stabilized through a combination of energy-lowering MnF_6 octahedral rotations and Jahn-Teller (JT) bond elongations; the latter arise to remove the orbital degeneracy owing to electron occupation of the majority spin $e_g^{\uparrow}$ manifold presented by a cubic crystal field. These combined effects produce a crystal structure at ambient pressure that exhibits elongated Mn-F bonds along the long, crystallographic c axis depicted in Fig. 2(b) and is common for manganates with axial ratios $c/a > 1$ [44,45].

Upon application of hydrostatic pressure, we find a reorientation of the long JT Mn-F bond occurs for unit cell volumes of 240 ± 0.1 Å^3, corresponding to an experimental pressure between 2.10 and 2.15 GPa, in agreement with Ref. [31]. At the electronic structure level, we find that the low-pressure fluoromanganate phases have fully occupied $d_{z^2-r^2}$ orbitals, whereas in the high-pressure phase, the occupancy reverses to be predominately of $d_{x^2-y^2}$ orbital character. Unlike previously reported IPTs in manganites, the JT mode is always present and the strong orbital-lattice coupling facilitates the electronic transition, which is marked by a giant (70%) change in the orbital polarization of the Mn e_g manifold through a renormalization of the mode stiffness of the JT distortion. Uncovering the microscopic origins of the transition sheds light on the effect of stress on the magnetic, electronic, and structural degrees of freedom in Na_3MnF_6, but more broadly it reveals that the JT distortion need not be removed across such transitions and hence a well-defined orbitally ordered state may exist across such phase boundaries in related phases.

II. COMPUTATIONAL AND SIMULATION DETAILS

We performed density functional theory calculations with the general gradient approximation (GGA) of Perdew-Burke-Ernzerhof revised for solids [46] (PBEsol) as implemented in the Vienna *Ab initio* Simulation Package (VASP) [47,48] with the projector augmented wave (PAW) method [49] to treat the core and valence electrons using the following valence configurations: $2p^6 3s^1$ for Na, $3p^6 4s^1 3d^6$ for Mn, and $2s^2 2p^5$ for F. We used a $7 \times 7 \times 7$ Monkhorst-Pack k-point mesh [50] with Gaussian smearing (0.1 eV width) for the Brillouin zone (BZ) integrations and a 600-eV plane-wave cutoff. Spin-polarized structural relaxations were performed until the Hellmann-Feynman forces were less than 1 meV Å^{-1} for each atom position.

Magnetic order. The long-range spin order for Na_3MnF_6 has not been previously reported. Therefore, prior to carrying out the pressure study, we explored the energetics for A-type antiferromagnetic order (in-plane ferromagnetic coupling between Mn sites and out-of-plane antiferromagnetic coupling) and ferromagnetic order on the monoclinic $P2_1/n$ (ambient) structure with the JT Mn-F bond directed along the c axis.

These two magnetic configurations are compatible with the 20-atom unit cell used in all calculations. From our total energy calculations of the fully relaxed phases, we find that the ferromagnetic configuration is essentially degenerate with the antiferromagnetic configuration: There is less than 0.1% difference in cell volume and an energy difference of 0.4 meV per formula unit (f.u.). These small differences between the magnetic variants also persist for calculations performed at elevated pressures. Owing to the strong ionic character of the fluoride and the fact that there appears to be very weak spin-lattice coupling, we use structures with ferromagnetic (FM) order throughout to perform the hydrostatic pressure simulations. As described below, the FM order yields excellent agreement with experimental structural data.

Application of hydrostatic pressure. We computationally mimic the experimental hydrostatic pressure study by imposing the lattice constants and monoclinic angles reported in Ref. [31], while allowing the internal coordinates to fully relax to obtain the total energies for both the low-pressure ($[P2_1/n]_1$) and the high-pressure ($[P2_1/n]_2$) phases. Throughout we distinguish between the two phases by using the space-group label with an additional index, 1 or 2, appended to the end to indicate if it is the low-pressure (phase 1) or high-pressure (phase 2) Na_3MnF_6 structure. The starting atomic configuration for the $[P2_1/n]_1$ phases employs the positions obtained from our fully relaxed zero-pressure DFT-PBEsol simulations, whereas for the $[P2_1/n]_2$ structural relaxations, we initialize the atomic positions to those reported experimentally [31].

TABLE I. Comparison between the internal coordinates given in reduced units and lattice parameters a, b, and c (Å) for monoclinic Na_3MnF_6 ($P2_1/n$) obtained from DFT-PBEsol calculations and x-ray synchrotron experiments [30]. The monoclinic angle, $\beta = 88.96^\circ$, is constrained to the experimental value. The unit cell volumes obtained from DFT and experiment are 251.09 and 250.97 Å^3, respectively. The Mn and Na(1) cations occupy the Wyckoff positions (WPs) $2a(0,0,0)$ and $2b(0,0,1/2)$, respectively, without free parameters, while all other atoms are free to displace.

Atom	WP		PBEsol	Experiment [30]
Na(2)	4*e*	*x*	0.510	0.509
		y	0.058	0.055
		z	0.750	0.750
F(1)	4*e*	*x*	0.122	0.115
		y	−0.063	−0.058
		z	0.761	0.767
F(2)	4*e*	*x*	0.722	0.719
		y	0.828	0.829
		z	−0.058	−0.053
F(3)	4*e*	*x*	0.162	0.163
		y	0.724	0.721
		z	0.068	0.067
a			5.472	5.471
b			5.684	5.683
c			8.075	8.073

III. RESULTS

A. Na_3MnF_6 equilibrium structure

Before performing the hydrostatic pressure study on Na_3MnF_6, we first determine the equilibrium structure at zero pressure with ferromagnetic spin order. Consistent with experiments, we find a distorted monoclinic structure with in-phase MnF_6 octahedral rotations about the c axis and out-of-phase tilts. The combination of rotations and tilts gives the $a^-a^-c^+$ tilt pattern as described within Glazer notation [51]. Table I shows that the PBEsol functional provides an accurate description of the structural parameters of Na_3MnF_6 when compared to experiment. The error in the cell volume is ∼0.05%, under the constraint that the PBEsol structure has the same monoclinic angle as that reported in Ref. [30].

To understand the complex atomic distortions in the monoclinic phase, we first recognize that a group-subgroup relationship exists between the ideal high-symmetry cubic structure without octahedral distortions or rotations, $Fm\bar{3}m$, and the $P2_1/n$ structure [52]. Mode-crystallographic analysis [53,54] then enables us to determine the full set of unique symmetry-adapted mode displacements active in the $Fm\bar{3}m \rightarrow P2_1/n$ transition (see Fig. 3 for schematic illustrations), described as irreducible representation (irreps) of $Fm\bar{3}m$. We find that the cubic-to-monoclinic symmetry reduction requires a combination of at least two of these modes; based on the physical character (Fig. 3) and distortion mode amplitudes (Table SI of the Supplementary Material available in Ref. [25]) of the modes present in the ground-state structure, we deduce that the symmetry reduction is driven by out-of-phase octahedral rotations about the b axis and in-phase rotations about the c axis, i.e., $\Gamma_4^+ \oplus X_3^+$.

B. Hydrostatic pressure-induced isosymmetric transition

We investigate phase stability of the monoclinic Na_3MnF_6 by computing the total energy at various volumes for both the $[P2_1/n]_1$ and $[P2_1/n]_2$ structures [55]. Figure 4 shows that the energy of both monoclinic phases increases with increasing pressure (decreasing cell volume). At low pressure $[P2_1/n]_1$, exhibiting the JT bond axis oriented along the c axis, is more stable than $[P2_1/n]_2$ (JT bond axis in the ab plane) by ∼20 meV. This energetic stability remains until near the unit cell volume of 240 Å, where we find that both monoclinic structures are stable within our simulations. Upon further increase in pressure, $[P2_1/n]_2$ is stabilized relative to $[P2_1/n]_1$ by nearly the same energetic difference. From our mode-crystallographic analyses, we find that the Q_3 irrep has the largest response at the transition, exhibiting both a discontinuity and a sign change [Fig. 4 (inset)]. (We explore the energetics of this mode in more detail below.) We observe no change in space-group symmetry or occupied Wyckoff positions for all volumes computed, consistent with available experimental results, which makes this transition isosymmetric.

We now explore changes in the internal atomic positions with pressure, focusing on the cooperative behavior of the Mn-F octahedra. We first examine the changes in the Mn-F bond lengths. Rather than using the symmetry-mode description, we parametrize the structural distortions to the MnF_6 octahedra in terms of first-order Jahn-Teller (JT) elongations Q_2 and

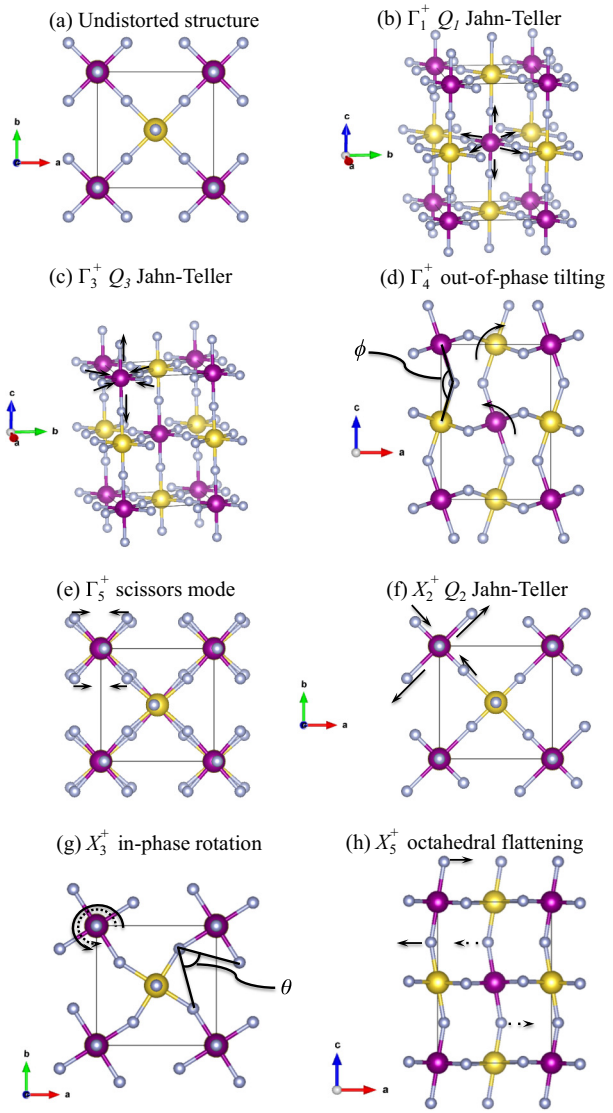

FIG. 3. (Color online) Illustration of symmetry-adapted mode displacements which appear in monoclinic Na_3MnF_6 labeled according to irreps of the undistorted (a) $Fm\bar{3}m$ structure. (b) Γ_1^+, the Q_1 JT mode commonly referred to as the breathing distortion. (c) Γ_3^+, the Q_3 (two-out–four-in) JT vibrational mode. (d) Γ_4^+, the out-of-phase tilting of octahedra about the b axis. The tilt angle is measured as $(180^\circ - \phi)/2$. (e) Γ_5^+, "scissor" mode which brings equatorial F anions in the MnF_6 octahedra closer together and reduces the intra-octahedral F-Mn-F bond angle from the ideal 90°. (f) X_2^+, the Q_2 (two-in–two-out) bond stretching mode in the ab plane. (g) X_3^+, in-phase rotations of the octahedra about the c axis. The rotation angle is measured as $(90^\circ - \theta)/2$. (h) X_5^+, antiparallel apical F displacements which lead to a flattening of the MnF_6 octahedra. Note that the Na(2) cations are omitted for clarity throughout, and broken lines indicate atomic displacements in the layer below.

Q_3 [56]. This allows us to describe the JT modes by the position of the surrounding ligands in an octahedral field whose normal coordinates are associated with the vibrational mode that leads to a crystalline field removing the orbital degeneracy. The Q_2 mode is a tetragonal "two-in and two-out" bond distortion in the ab plane [$Q_2 > 0$, Fig. 3(f)], while Q_3

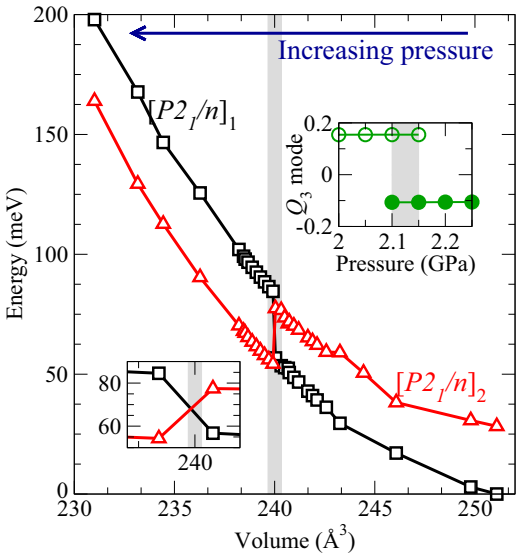

FIG. 4. (Color online) Evolution of the total energy for the monoclinic $[P2_1/n]_1$ and $[P2_1/n]_2$ structures with cell volume given relative to the relaxed 0 K $[P2_1/n]_1$ ground-state structure. The shaded region highlights the pressure domain of phase coexistence and the transition point about which the stability of the monoclinic phases reverses (see left inset). The right inset shows the evolution of the Q_3 JT mode with pressure near the transition.

is a three-dimensional "two-out and four-in" bond distortion [$Q_3 > 0$, Fig. 3(c)].

In Na_3MnF_6, the Q_2 and Q_3 vibrational modes are ferrodistortively aligned. In the monoclinic systems studied here, the $Q_2 > 0$ mode elongates the Mn-F bonds that lie mainly along the b axis and shortens those along a, while $Q_3 > 0$ shortens the Mn-F bonds in the ab plane while elongating the bonds along c axis.

We obtain the fraction of the Q_2 and Q_3 JT modes present in the stable monoclinic low- and high-pressure variants as a function of hydrostatic pressure by computing the magnitude of the JT normal modes as follows:

$$Q_2 = \frac{2}{\sqrt{2}}[\mathrm{F}(3) - \mathrm{F}(2)],$$

$$Q_3 = \frac{2}{\sqrt{6}}[2\mathrm{F}(1) - \mathrm{F}(2) - \mathrm{F}(3)],$$

where, F(1), F(2), and F(3) are the Mn-F bond lengths directed along the c, a, and b axes, respectively. The JT phase is defined by $\Theta = \tan^{-1} Q_2/Q_3$. Within this formalism, $\Theta = 0^\circ$ represents a JT distortion of octahedra stretched along the c axis. Angles of $\Theta = \pm 120^\circ$ correspond to JT distortions along the b and a axis, respectively [44,45,57].

Figure 5 shows the stability of the monoclinic Na_3MnF_6 structures in the Q_2-Q_3 plane. For $[P2_1/n]_1$, $\Theta = 2.99^\circ$ at ambient pressure and evolves to a maximum of value of 4.06° at the critical pressure. Thus, in the low-pressure Na_3MnF_6 phase, the Q_3 JT mode dominates the Q_2 mode, leading to a tetragonal distortion of the MnF_6 octahedra that also elongates the c axis and contracts the crystal in the ab plane. Across the IPT there are no intermediate values of Θ (grayed region).

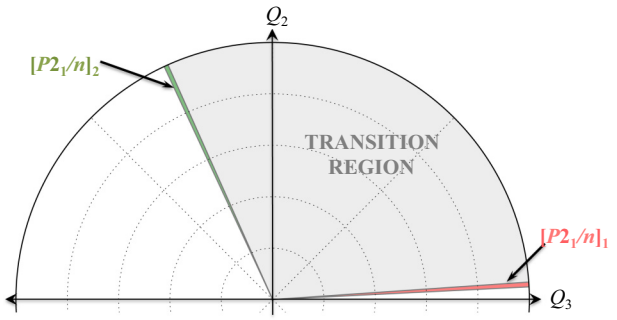

FIG. 5. (Color online) Phase stability of $[P2_1/n]_1$ and $[P2_1/n]_2$ represented in the Q_2-Q_3 plane of the JT lattice distortions. The red, green, and gray wedges illustrate the stability regions for $[P2_1/n]_1$, $[P2_1/n]_2$, and the transition region, revealing that each structure is characterized by a dominant Q_2 or Q_3 mode.

In the high-pressure phase $[P2_1/n]_2$, a drastic increase in the value of Θ occurs, i.e., $\Theta = 114.1^\circ$, and reaches a maximum of $\Theta = 115.0^\circ$, which suggests a first-order transition to a Q_2-type JT distortion and is consistent with the long bond becoming the Mn-F(3) bond as observed in the $[P2_1/n]_2$ phase.

C. Jahn-Teller electronic effects

We now investigate the electronic structure evolution across the IPT to understand the coupling between the electron and lattice degrees of freedom in Na_3MnF_6. Here Mn(III) is found in a high-spin d^4 configuration with one electron in the e_g manifold, which appears as a strong JT distortion in the octahedra [58–60]. Thus, we anticipate that hydrostatic pressure directly affects the value of Θ in the Q_2-Q_3 subspace. Importantly, the value of Θ also provides a measure of the average character of the occupied molecular orbital state $|\Theta\rangle$ of the JT ion for a given static cooperative JT distortion as an arbitrary superposition of the e_g orbital wave functions [44,61]. It can be approximated for a system at absolute zero as [57]

$$|\Theta\rangle = \cos(\Theta/2)|d_{z^2-r^2}\rangle + \sin(\Theta/2)|d_{x^2-y^2}\rangle.$$

We now use maximally localized Wannier functions (MLWFs) [62,63] to transform our periodic wave functions forming the valence band (VB) and conduction band (CB) edges into a local real-space representation of the e_g ($d_{x^2-y^2}$ and $d_{z^2-r^2}$) orbitals. The subspace is spanned by these atomiclike orbitals for the two Mn cations in the unit cell to evaluate the percent character of each orbital contributing to $|\Theta\rangle$.

Figure 6(a) shows the electronic band structure near the Fermi level (E_F) for $[P2_1/n]_1$ at ambient pressure. The occupied bands are largely $3d_{z^2-r^2}$-like Mn states while the $3d_{x^2-y^2}$ orbital forms the CB throughout the BZ. It is significant to note that $\Theta = 2.99^\circ$ for $[P2_1/n]_1$ at ambient pressure and this corresponds to $|\Theta\rangle$ being composed of 99.9% $d_{z^2-r^2}$ orbital character in agreement with the MLWF projection, Fig. 6(a). This result is characteristic of the orbital splitting anticipated with $Q_3 > 0$, where the apical bonds in the MnF_6 octahedra are elongated and the equatorial bonds contract [45]. The MLWFs reveal strong localization

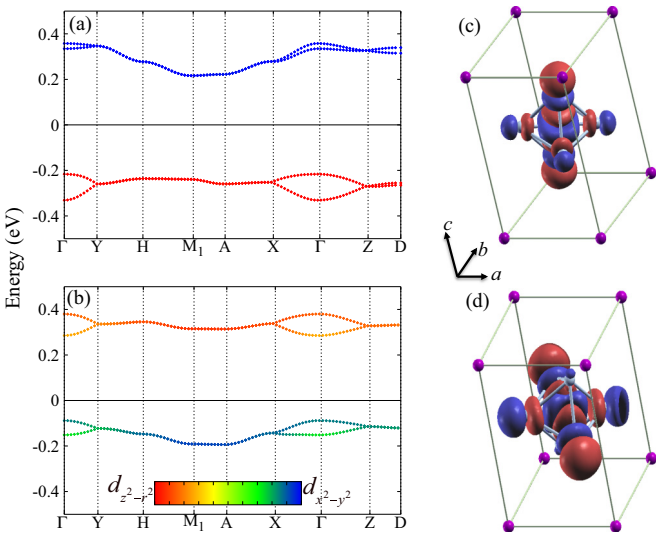

FIG. 6. (Color online) Low-energy electronic band structure about the Fermi level (horizontal line at 0 eV) with the projected e_g orbital character for Na_3MnF_6 at (a) $[P2_1/n]_1$ (0.0 GPa) and (b) $[P2_1/n]_2$ (2.5 GPa). The MLWF for the occupied molecular orbital for the (c) $[P2_1/n]_1$ and (d) $[P2_1/n]_2$.

of the atomic like $3d_{z^2-r^2}$ orbital on the Mn cations below E_F [Fig. 6(c)]; the majority spin $e_g^{\uparrow}$ electron occupies the orbital directed along the long JT-bond to reduce the Coulombic repulsion induced by the F $2p$ electron cloud.

Figure 6(b) depicts the electronic structure for $[P2_1/n]_2$ at 2.50 GPa. From the projection onto the MLWFs, we observe in the high-pressure phase that the VB and CB adopt mixed e_g-orbital character throughout the BZ. The occupied orbital, although dominated by atomic $d_{x^2-y^2}$ character, has an admixture of $d_{z^2-r^2}$ [Fig. 6(d)]. At 2.50 GPa, $\Theta = 114.2^\circ$ in $[P2_1/n]_2$ and this angle predicts a wave function with 29.5% $d_{z^2-r^2}$ orbital character, a 70% change in the orbital polarization. The mixed e_g molecular orbital state is typical for manganates with a Q_2-like JT distortion; i.e., the long-JT bond axis is oriented in the ab plane [45,64,65].

We now examine the energetics associated with the changes in $|\Theta\rangle$ by computing the Q_2-Q_3 energy surface (Fig. 7). We achieve this by incrementally increasing the Q_2 (X_2^+) and Q_3 (Γ_3^+) symmetry-adapted mode amplitudes in the $[P2_1/n]_1$ phase at ambient pressure [25] and $[P2_1/n]_2$ at 2.50 GPa (Table II) with respect to the undistorted reference structures [66]. In Fig. 7, mode amplitudes of $Q_2 > 0$ represent a JT distortion which elongates the Mn-F(3) bond and shortens the Mn-F(2) bonds in the ab plane, while $Q_2 < 0$ shortens Mn-F(3) and elongates Mn-F(2). Similarly, $Q_3 > 0$ mode amplitudes correspond to a two-out–four-in JT distortion, which stretches the apical Mn-F(1) while shortening the Mn-F(2) and Mn-F(3) equatorial bonds. Conversely, $Q_3 < 0$ gives the four-out–two-in JT bonding environment that elongates bonds in the ab plane [Mn-F(2) and Mn-F(3)] and shortens the Mn-F(1) bond.

Considering only JT modes in the equilibrium volume of $[P2_1/n]_1$ at ambient pressure, we find a single energy minimum at $Q_3 \sim 0.11$ and $Q_2 = 0$ [Fig. 7(a)]. In this phase, a two-out–four-in Q_3 JT vibrational mode stabilizes Na_3MnF_6

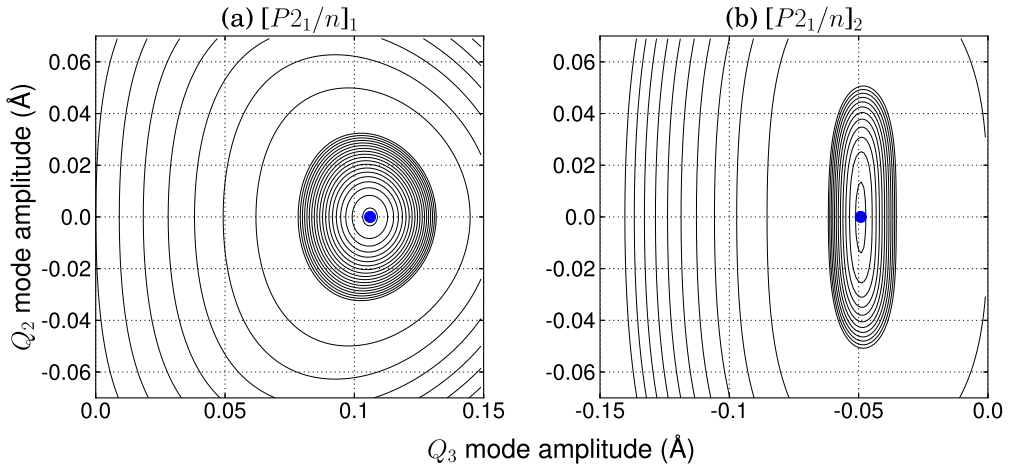

FIG. 7. (Color online) Calculated two-dimensional energy surface contours for (a) $[P2_1/n]_1$ at ambient pressure and (b) $[P2_1/n]_2$ at 2.50 GPa with respect to the amplitude of the Q_2 and Q_3 JT modes derived from mode crystallography. The solid (blue) circles denote the position of minima in the potential energy surface.

at ambient pressure by approximately 38.6 meV/f.u. over the undistorted phase, which is consistent with the structural and electronic investigations already described. Despite having a small finite amplitude of Q_2 (X_2^+) present in the equilibrium structure [25], Fig. 7(a) indicates that in the absence of other distortions any nonzero amplitude of Q_2 leads to an energetic penalty in $[P2_1/n]_1$. Thus, an asymmetric Mn-F bond stretching in the *ab* plane is an unfavorable distortion at ambient conditions without the presence of another distortion.

From Fig. 7(b), we observe that our two-dimensional energy surface predicts a single energy minimum for $[P2_1/n]_2$ at 2.50 GPa. Here the minimum is located at $Q_3 \sim -0.048$ and $Q_2 = 0$. In the stable $[P2_1/n]_2$ phase it is noteworthy that the stability regime for the Q_3 vibrational mode is in a negative range. This indicates that unlike the $[P2_1/n]_1$ phase, at high pressures beyond the IPT a four-out–two-in Q_3 and not a two-out–four-in Mn-F distortion is required to stabilize the structure. According to the JT theory, a d^4 cation with $Q_3 < 0$ distortion splits the e_g degeneracy by occupying the $d_{x^2-y^2}$ orbital. Thus, the change in sign of the Q_3 mode is in accord with the $d_{x^2-y^2}$ state forming the VB edge as observed in our calculations (Fig. 6). However, since $Q_2 = 0$ in the absence of any other distortion, at high-pressure Na_3MnF_6 would exhibit four equivalent equatorial bonds, i.e., Mn-F(2) = Mn-F(3), in the reduced subspace. The latter is in contrast to the fully relaxed atomic and electronic structure of the $[P2_1/n]_2$ phase. The MnF_6 octahedra exhibit multiple distortions with an approximately $Q_2 > 0$-like JT bonding environment. Indeed, the symmetry-adapted mode amplitudes for Na_3MnF_6 at 2.50 GPa (Table II) indicate that the Q_2 mode (X_2^+) is finite and larger in amplitude ($Q_2 = 0.083$) than at ambient pressure ($Q_2 = 0.056$).

TABLE II. Symmetry-adapted mode amplitudes (in Å) present in the equilibrium Na_3MnF_6 $[P2_1/n]_2$ phase at 2.50 GPa obtained from DFT-PBEsol calculations. The mode amplitudes are normalized with respect to the parent $Fm\bar{3}m$ structure.

Mode	Space group (number)	DFT-PBEsol
Γ_1^+	$Fm\bar{3}m$ (225)	0.119
Γ_3^+	$I4/mmm$(139)	0.103
Γ_4^+	$C2/m$ (12)	1.465
Γ_5^+	$C2/m$(12)	0.219
X_2^+	$P4_2/mnm$ (136)	0.083
X_3^+	$P4/mnc$(128)	0.892
X_5^+	$Pnnm$ (58)	0.786

We now seek to identify which other structural distortion (non-JT) acts to stabilize nonzero Q_2 mode amplitudes in the equilibrium structures. From the mode decomposition analysis at ambient and elevated pressure, we observe that the largest contribution to the equilibrium structures arise from the tilt (Γ_4^+) and rotation (X_3^+) of the MnF_6 units. To understand the nature of the tilt-Q_2 and rotation-Q_2 coupling, we incrementally increase the mode amplitude of Q_2 at finite amplitudes of the tilt and rotation (0%, 50%, 80%, 90%, and 100% of their maximum) with respect to the undistorted reference structure.

Figure 8 shows that both the tilt and rotation modes couple to Q_2 and give a net energy gain in the total energy in both pressure regimes at finite amplitude. From Fig. 8(a) we observe that as the amplitude of tilt distortion increases in $[P2_1/n]_1$, the curvature of the Q_2 free energy evolves from a positive parabola with a single minimum at the $Q_2 = 0$ to a double-well potential with negative curvature about the origin and minima at finite Q_2 for tilt amplitudes $\geqslant$80%. This signifies a continuous softening of the Q_2 phonon mode induced by large amplitudes of the tilt mode (Γ_4^+ irrep), which effectively stabilizes the finite value of the asymmetric stretching observed in the ground state. It occurs through a fourth-order biquadratic anharmonic interaction that renormalizes the mode stiffness of the quadratic Q_2^2 mode. The behavior of the MnF_6 rotation-Q_2 coupling in Fig. 8(b) shows that there is a large energetic gain associated with increasing amplitudes of the rotation mode. The single minima of the parabolic energy curves indicate, however, that while this coupling contributes to the total energy it does not soften the Q_2 mode frequency, but rather shifts the mode amplitude of Q_2 to a nonzero value through a linear-quadratic interaction.

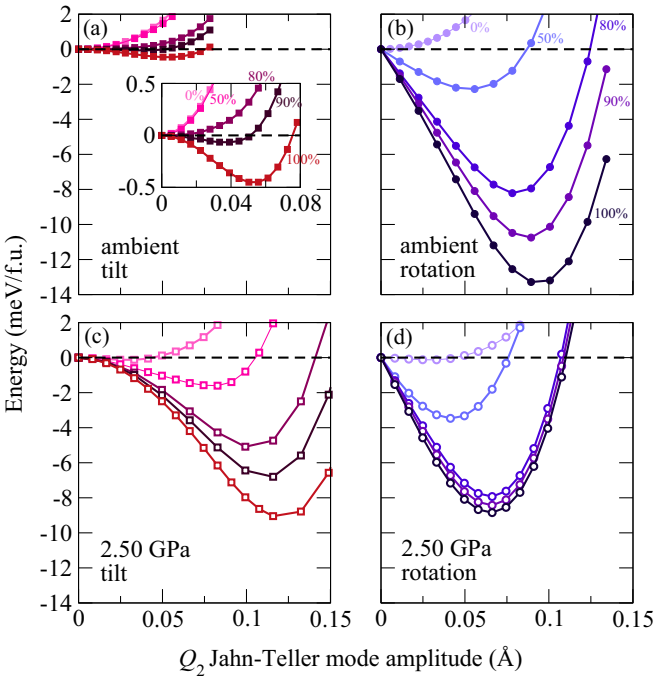

FIG. 8. (Color online) Energy evolution from the coupling of the Q_2 JT distortion to the tilt and rotation at (a) and (b) ambient pressure (solid symbols) and at (c) and (d) 2.50 GPa (open symbols), respectively. Normalized energy gain obtained by increasing the amplitude of the Q_2 mode at fixed percentages of the out-of-phase tilt [panels (a) and (c)] and in-phase rotations [panels (b) and (d)] found in the ground equilibrium structures.

In the high-pressure phase (2.50 GPa) [Figs. 8(c) and 8(d)], we observe that the Q_2 irrep is unstable with a small energy gain <1 meV at both 0% tilt and rotation amplitudes. Figure 8(c) shows that increasing the amplitude of the tilt distortion in $[P2_1/n]_2$ leads to an enhanced energy stabilization, which ultimately promotes a larger Q_2 distortion in the high-pressure phase. In contrast, increasing the contribution of the rotational mode hardens the Q_2 mode, the negative curvature at the origin is lost as shown in [Fig. 8(d)] and leads to a smaller amplitude of Q_2 through the coupled $Q_2^2 Q_{X_3^+}$ interaction.

IV. DISCUSSION

Our calculations and structural analysis indicate that the IPT is due to the spontaneous redistribution of the electronic charge density among the e_g orbitals of the strong JT Mn cation. There is a change in orbital occupation between the two isostructural variants owing to the persistent JT distortion across the transition. Specifically, we find that at low values of hydrostatic pressure the system is stabilized with the long bond along the c axis with a filled $d_{z^2-r^2}$ orbital, which is characteristic of a $Q_3 > 0$ JT, where $c/a > 1$ [44,45]. Mode-crystallographic analysis coupled with phenomenological Landau investigations of the JT Mn-F bond distortions reveals that the lattice strain induced by hydrostatic pressure renormalizes the mode stiffness of the JT vibrational modes across the transition. The leading coefficient of the harmonic Q_3^2 term of Hamiltonian changes sign under hydrostatic pressure.

Most significantly, we observe that across the transition the Q_3 JT irrep switches from a two-out–four-in ($Q_3 > 0$) in $[P2_1/n]_1$ to a four-out–two-in ($Q_3 < 0$) in the $[P2_1/n]_2$ phase. While the key structural signature defining $[P2_1/n]_2$ is a Q_2-like Mn-F bonding arrangement, we contend that the primary factor in the stabilization of the high-pressure phase in Na_3MnF_6 is the change in sign of the Q_3 distortion mediated by the Q_2-MnF_6 tilt interaction. Table SI in the Supplemental Material [25] and Table II clearly show that the rotation amplitude is unchanged under pressure. Our electronic and phenomenological investigations indicate that at high pressure, it is more favorable for the charge to localize in the $d_{x^2-y^2}$-like orbital. Thus, the characteristic Q_2-like Mn-F_6 bonding distortion that differentiates the $[P2_1/n]_2$ and $[P2_1/n]_1$ phases is stabilized by second-order effects. We show that a strong coupling exists between the tilt and Q_2 lattice degrees of freedom owing to an anharmonic interaction that stabilizes finite amplitudes of Q_2 in the equilibrium structures. The importance of this secondary effect is highlighted by comparing [Figs. 8(a) and 8(c)], as the energetic gain produced by the tilt-Q_2 coupling is increased approximately 20× in the $[P2_1/n]_2$ phase at equilibrium over the ambient case.

In addition, our electronic structure calculations show that hydrostatic pressure has an effect on the crystal field splitting in the stable phases of Na_3MnF_6. We observe that the energy gap between the filled $d_{z^2-r^2}$ and the unoccupied $d_{x^2-y^2}$ is reduced from 0.43 eV at ambient pressure to 0.34 eV at the transition. Across the critical pressure for the transition, the band gap is 0.37 eV at 2.20 GPa. The continued application of hydrostatic pressure in the high-pressure phase further decreases the band gap at approximately 0.02 eV/GPa, which allows us to predict an insulator-to-metal transition around ∼20 GPa.

Based on this understanding, we performed a similar set of calculations for the d^0 compound Na_3ScF_6, which also

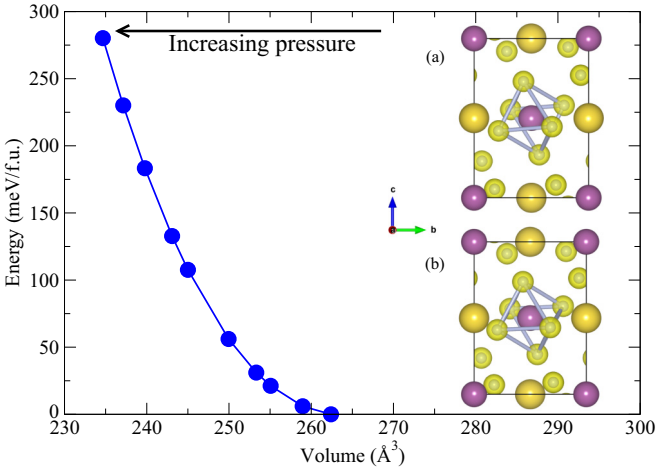

FIG. 9. (Color online) Evolution of the total energy of Na_3ScF_6 with cell volume relative to the DFT relaxed ground-state structure. The inset depicts the partial charge density obtained over the energy window ranging from −2 eV to E_F at (a) ambient pressure (0.0 GPa) and (b) 6.82 GPa. Unlike Na_3MnF_6, neither a structural transition nor a charge redistribution is observed.

crystallizes with $P2_1/n$ symmetry and for which experimental structural data under hydrostatic pressure exists [67]. We find there is no discontinuity in either the total energies (Fig. 9) or in the evolution of the Sc-F bond lengths up to a pressure of 6.82 GPa, which indicates that no isosymmetric transitions occur up to a pressure that is approximately 4.7 GPa higher than required for the fluoromanganate. Indeed, Fig. 9 shows the partial charge density for Na_3ScF_6 obtained by integrating over a finite region from -2 eV to E_F is highly uniform at both ambient pressure [Fig. 9(a)] and high pressure [Fig. 9(b)]. The absence of both a JT instability and an anisotropic bonding environment is consistent with the experimental findings and the proposed electronic origin for the IPT in Na_3MnF_6, highlighting the importance of the JT-active Mn(III).

V. CONCLUSION

We used first-principles density functional calculations to study the electronic and atomic origins of the first-order pressure-induced phase transition in Na_3MnF_6. We identified that the isosymmetric transition originates from two key features present in the fluoromangante: (i) a JT active Mn(III) ion with an e_g orbital degeneracy and (ii) the strong coupling of the cooperative Mn-F bond distortions with hydrostatic pressure. We observe that while simple structural arguments may identify the $[P2_1/n]_1$ phase of Na_3MnF_6 as being dominated by a Q_3-type JT distortion and the $[P2_1/n]_2$ phase as Q_2 type, the combined effect of both distortions with collective MnF_6 tilts are essential to describing the stability of the structure at ambient and hydrostatic pressures.

In the $[P2_1/n]_1$ structures the $Q_3 > 0$ JT distortion splits the e_g manifold into atomiclike occupied $d_{z^2-r^2}$ and an unoccupied $d_{x^2-y^2}$ orbitals owing to an elongated JT Mn-F bond aligned along the crystallographic c axis. After the transition to the high-pressure phase $[P2_1/n]_2$, the JT-bond axis reorients into the ab plane with the structure largely characterized by a Q_2-type bonding arrangement. The transition above 2.15 GPa is arguably driven by a spontaneous renormalization of the Q_3 vibrational mode; i.e., $Q_3 < 0$. The equilibrium structure of the $[P2_1/n]_2$ phase is stabilized by secondary lattice effects which couple the tilt and Q_2 JT phonon modes to give the Mn-F(3) > Mn-F(1) > Mn-F(2), which is the signature of the high-pressure phase of Na_3MnF_6.

This mechanism for the IPT drives an orbital reconstruction within the occupied $3d$ manifold of Mn^{3+}, whereby the JT distortion is always present in the structure. While it is understood that fluctuations in the orbital occupancy of the d orbitals can alter physical properties and drive structural transitions [68], this study presents an interesting case were the orbital degrees of freedom are highly sensitive to the mechanical boundary conditions owing to the cryolite structure. Finding materials where it is possible to induce large changes in orbital polarization is an active area of research, because even small changes in orbital occupations, particularly in thin films at surfaces and interfaces [69–72], can produce drastic variations in magnetic and transport properties. Given the large orbital reconstruction we observe with hydrostatic pressure, we anticipate that our study will motivate new synthetic efforts focused on exploring Na_3MnF_6 and related magnetic cryolites in thin film form. Electronic structure calculations focused on evaluating the feasibility of epitaxial strain to induce the IPT are in progress.

ACKNOWLEDGMENTS

N.C. thanks Danilo Puggioni for useful discussions. N.C. and J.M.R. acknowledge the donors of The American Chemical Society Petroleum Research Fund for support (Grant No. 52138-DNI10). DFT calculations were performed on the high-performance computing facilities available at the Center for Nanoscale Materials (CARBON Cluster) at Argonne National Laboratory, supported by the U.S. DOE, Office of Basic Energy Sciences (BES), Grant No. DE-AC02-06CH11357, and at the Extreme Science and Engineering Discovery Environment (XSEDE), which is supported by National Science Foundation Grant No. OCI-1053575.

[1] R. A. F. Pinlac, C. L. Stern, and K. R. Poeppelmeier, Crystals **1**, 3 (2011).
[2] A. T. Mulder, N. A. Benedek, J. M. Rondinelli, and C. J. Fennie, Adv. Funct. Mater. **23**, 4810 (2013).
[3] L. Qiao, K. H. L. Zhang, M. E. Bowden, T. Varga, V. Shutthanandan, R. Colby, Y. Du, B. Kabius, P. V. Sushko, M. D. Biegalski, and S. A. Chambers, Adv. Func. Mater. **23**, 2953 (2013).
[4] L. Martin and R. Ramesh, Acta Mater. **60**, 2449 (2012).
[5] J. M. Rondinelli, S. J. May, and J. W. Freeland, MRS Bull. **37**, 261 (2012).
[6] M. Imada, A. Fujimori, and Y. Tokura, Rev. Mod. Phys. **70**, 1039 (1998).
[7] J. B. Goodenough, Chem. Mater. **26**, 820 (2014).
[8] D. G. Schlom, L.-Q. Chen, X. Pan, A. Schmehl, and M. A. Zurbuchen, J. Amer. Ceram. Soc. **91**, 2429 (2008).
[9] L. W. Martin, S. P. Crane, Y.-H. Chu, M. B. Holcomb, M. Gajek, M. Huijben, C.-H. Yang, N. Balke, and R. Ramesh, J. Phys.: Condens. Matter **20**, 434220 (2008).
[10] V. M. Goldschmidt, Naturwissenschaften **14**, 477 (1926).
[11] M. T. Anderson, K. B. Greenwood, G. A. Taylor, and K. R. Poeppelmeier, Prog. Solid State Chem. **22**, 197 (1993).
[12] G. King and P. M. Woodward, J. Mater. Chem. **20**, 5785 (2010).
[13] T. Saha-Dasgupta, J. Phys.: Condens. Matter **26**, 193201 (2014).
[14] J. Young and J. M. Rondinelli, Chem. Mater. **25**, 4545 (2013).
[15] O. Erten, O. N. Meetei, A. Mukherjee, M. Randeria, N. Trivedi, and P. Woodward, Phys. Rev. Lett. **107**, 257201 (2011).
[16] D. D. Sarma, P. Mahadevan, T. Saha-Dasgupta, S. Ray, and A. Kumar, Phys. Rev. Lett. **85**, 2549 (2000).
[17] O. N. Meetei, O. Erten, M. Randeria, N. Trivedi, and P. Woodward, Phys. Rev. Lett. **110**, 087203 (2013).
[18] J. Ravez, J. Phys. III **7**, 1129 (1997).

[19] C. Ederer and N. A. Spaldin, Phys. Rev. B **74**, 020401 (2006).
[20] J. F. Scott and R. Blinc, J. Phys.: Condens. Matter **23**, 113202 (2011).
[21] A. C. Garcia-Castro, N. A. Spaldin, A. H. Romero, and E. Bousquet, Phys. Rev. B **89**, 104107 (2014).
[22] J. Rau, K. Aliouane, M. Hamadne, A. Guehria, M. E. Omari, J. Grannec, and J. Ravez, Solid State Ionics **127**, 301 (2000).
[23] A. Tressaud, J. Portier, S. Shearer-Turrell, J.-L. Dupin, and P. Hagenmuller, J. Inorg. Nucl. Chem. **32**, 2179 (1970).
[24] G. King, A. M. Abakumov, P. M. Woodward, A. Llobet, A. A. Tsirlin, D. Batuk, and E. V. Antipov, Inorg. Chem. **50**, 7792 (2011).
[25] See Supplemental Material at http://link.aps.org/supplemental/10.1103/PhysRevB.90.094114 for discussion of tolerance factor in double pervoskite fluorides and additional mode amplitude data of the equilibrium phase.
[26] F. C. Hawthorne and R. B. Ferguson, Can. Mineral. **13**, 377 (1975).
[27] L. R. Moras, J. Inorg. Nucl. Chem. **36**, 3876 (1974).
[28] I. Flerov, M. Gorev, K. Aleksandrov, A. Tressaud, J. Grannec, and M. Couzi, Mater. Sci. Eng., R **24**, 81 (1998).
[29] W. Massa and D. Babel, Chem. Rev. **88**, 275 (1988).
[30] U. Englich, W. Massa, and A. Tressaud, Acta Crystallogr., Sect. C: Cryst. Struct. Commun. **48**, 6 (1992).
[31] S. Carlson, Y. Xu, U. Hlenius, and R. Norrestam, Inorg. Chem. **37**, 1486 (1998).
[32] J. F. Scott, Adv. Mater. **22**, 2106 (2010).
[33] M. T. Dove, *Introduction to Lattice Dynamics* (Cambridge University Press, Cambridge, UK, 1993).
[34] A. G. Christy, Acta Crystallogr., Sect. B: Struct. Sci. **51**, 753 (1995).
[35] A. S. Gibbs, K. S. Knight, and P. Lightfoot, Phys. Rev. B **83**, 094111 (2011).
[36] Z. Chen, Z. Luo, C. Huang, Y. Qi, P. Yang, L. You, C. Hu, T. Wu, J. Wang, C. Gao, T. Sritharan, and L. Chen, Adv. Funct. Mater. **21**, 133 (2011).
[37] H. M. Christen, J. H. Nam, H. S. Kim, A. J. Hatt, and N. A. Spaldin, Phys. Rev. B **83**, 144107 (2011).
[38] J. M. Rondinelli and S. Coh, Phys. Rev. Lett. **106**, 235502 (2011).
[39] G. Gou and J. M. Rondinelli, Adv. Mater. Interfaces **1**, 1400042 (2014).
[40] A. J. Hatt, N. A. Spaldin, and C. Ederer, Phys. Rev. B **81**, 054109 (2010).
[41] T.-Y. Tan, Q. Zhou, B. J. Kennedy, Q. Gu, and J. A. Kimpton, Solid State Sci. **14**, 506 (2012).
[42] S. Tripathi and V. Petkov, Appl. Phys. Lett. **102**, 061909 (2013).
[43] B. J. Kennedy, P. J. Saines, J. Ting, Q. Zhou, and J. A. Kimpton, J. Solid State Chem. **182**, 2858 (2009).
[44] K. I. Kugel and D. I. Khomski, Sov. Phys. Usp. **25**, 231 (1982).
[45] J. B. Goodenough, A. Wold, R. J. Arnott, and N. Menyuk, Phys. Rev. **124**, 373 (1961).
[46] J. P. Perdew, A. Ruzsinszky, G. I. Csonka, O. A. Vydrov, G. E. Scuseria, L. A. Constantin, X. Zhou, and K. Burke, Phys. Rev. Lett. **100**, 136406 (2008).
[47] G. Kresse and J. Furthmüller, Phys. Rev. B **54**, 11169 (1996).
[48] G. Kresse and D. Joubert, Phys. Rev. B **59**, 1758 (1999).
[49] P. E. Blöchl, Phys. Rev. B **50**, 17953 (1994).
[50] H. J. Monkhorst and J. D. Pack, Phys. Rev. B **13**, 5188 (1976).
[51] A. M. Glazer, Acta Crystallogr., Sect. B: Struct. Crystallogr. Cryst. Chem. **28**, 3384 (1972).
[52] The occupied Wyckoff sites for Na_3MnF_6 in the $Fm\bar{3}m$ space group are 4*a* for Mn, 4*b* for Na(1), 8*c* for Na(2), and 24*e* for F.
[53] B. J. Campbell, H. T. Stokes, D. E. Tanner, and D. M. Hatch, J. Appl. Crystallogr. **39**, 607 (2006).
[54] J. M. Perez-Mato, D. Orobengoa, and M. I. Aroyo, Acta Crystallogr., Sect. A: Found. Crystallogr. **66**, 558 (2010).
[55] Fine sampling near the reported [31] transition pressure is achieved by extrapolating best-fit lines of the evolution of lattice parameters from the energetically more stable $[P2_1/n]_2$.
[56] J. H. Van Vleck, J. Chem. Phys. **7**, 72 (1939).
[57] J. Kanamori, J. Appl. Phys. **31**, S14 (1960).
[58] M. A. Carpenter and C. J. Howard, Acta Crystallogr., Sect. B: Struct. Sci. **65**, 134 (2009).
[59] J. B. Goodenough, Rep. Prog. Phys. **67**, 1915 (2004).
[60] J. B. Goodenough, Annu. Rev. Mater. Sci. **28**, 1 (1998).
[61] A. Stroppa, P. Barone, P. Jain, J. M. Perez-Mato, and S. Picozzi, Adv. Mater. **25**, 2284 (2013).
[62] N. Marzari and D. Vanderbilt, Phys. Rev. B **56**, 12847 (1997).
[63] A. A. Mostofi, J. R. Yates, Y.-S. Lee, I. Souza, D. Vanderbilt, and N. Marzari, Comput. Phys. Commun. **178**, 685 (2008).
[64] J. E. Medvedeva, M. A. Korotin, V. I. Anisimov, and A. J. Freeman, Phys. Rev. B **65**, 172413 (2002).
[65] Y. Murakami, J. P. Hill, D. Gibbs, M. Blume, I. Koyama, M. Tanaka, H. Kawata, T. Arima, Y. Tokura, K. Hirota, and Y. Endoh, Phys. Rev. Lett. **81**, 582 (1998).
[66] The undistorted structures are constructed to have cell volumes and monoclinic angles that correspond to the pressure being studied with all mode amplitudes equal to zero relative to the DFT-PBEsol relaxed monoclinic structures. The energy maps are obtained from 225 self-consistent total energy calculations and then fitting these points to a polynomial expansion in orders of Q_2 and Q_3.
[67] S. Carlson, Y. Xu, and R. Norrestam, J. Solid State Chem. **135**, 116 (1998).
[68] Y. Tokura and N. Nagaosa, Science **288**, 462 (2000).
[69] T. Chatterji, F. Fauth, B. Ouladdiaf, P. Mandal, and B. Ghosh, Phys. Rev. B **68**, 052406 (2003).
[70] A. Tebano, C. Aruta, S. Sanna, P. G. Medaglia, G. Balestrino, A. A. Sidorenko, R. De Renzi, G. Ghiringhelli, L. Braicovich, V. Bisogni, and N. B. Brookes, Phys. Rev. Lett. **100**, 137401 (2008).
[71] M. J. Han, C. A. Marianetti, and A. J. Millis, Phys. Rev. B **82**, 134408 (2010).
[72] E. Benckiser, M. W. Haverkort, S. Brck, E. Goering, S. Macke, A. Fra, X. Yang, O. K. Andersen, G. Cristiani, H.-U. Habermeier, A. V. Boris, I. Zegkinoglou, P. Wochner, H.-J. Kim, V. Hinkov, and B. Keimer, Nat. Mater. **10**, 189 (2011).